



AIAA Paper 2001-1025

**CFD Validation Studies for Hypersonic
Flow Prediction**

**Peter A. Gnoffo
NASA Langley Research Center
Hampton, Virginia 23681-0001**

**39th AIAA Aerospace Sciences
Meeting & Exhibit**

8-11 January 2001 / Reno, NV



CFD Validation Studies for Hypersonic Flow Prediction

Peter A. Gnoffo[†]
p.a.gnoffo@larc.nasa.gov
NASA Langley Research Center
Hampton, VA 23681-0001

Abstract

A series of experiments to measure pressure and heating for code validation involving hypersonic, laminar, separated flows was conducted at the Calspan-University at Buffalo Research Center (CUBRC) in the Large Energy National Shock (LENS) tunnel. The experimental data serves as a focus for a code validation session but are not available to the authors until the conclusion of this session. The first set of experiments considered here involve Mach 9.5 and Mach 11.3 N₂ flow over a hollow cylinder-flare with 30° flare angle at several Reynolds numbers sustaining laminar, separated flow. Truncated and extended flare configurations are considered. The second set of experiments, at similar conditions, involves flow over a sharp, double cone with fore-cone angle of 25° and aft-cone angle of 55°. Both sets of experiments involve 30° compressions. Location of the separation point in the numerical simulation is extremely sensitive to the level of grid refinement in the numerical predictions. The numerical simulations also show a significant influence of Reynolds number on extent of separation. Flow unsteadiness was easily introduced into the double cone simulations using aggressive relaxation parameters that normally promote convergence.

Nomenclature

C_p	pressure coefficient, $2(p-p_\infty)/\rho_\infty V_\infty^2$
L	reference length from leading edge to junction
M	Mach number
\mathcal{M}	molecular weight, kg/k-mole
p	pressure, N/m ²
Pr	Prandtl number
q_w	wall heat transfer rate, W/m ²
Re	$\rho_\infty V_\infty L / \mu_\infty$, Reynolds number, m ⁻¹
s	arc length, mm
St	hypersonic approximation to Stanton number, $2q_w / \rho_\infty V_\infty^3$
T	temperature, K
T_v	vibrational temperature, K
u, v	velocity components in x and r directions, respectively, m/s
V_∞	free stream velocity, m/s
x, r	cylindrical coordinates, cm
ϵ	eigenvalue limiter
γ	specific heat ratio
μ	viscosity, kg/m-s
ρ	density, kg/m ³

Subscripts

att	attachment point, zero shear
i	stream wise coordinate direction
j	normal coordinate direction
sep	separation point, zero shear
w	wall surface conditions
∞	free stream conditions

Table Abbreviations

A	adapted grid, shock aligned
C	curve fit collision cross section
HCEF	hollow cylinder, extended flare
HCTF	hollow cylinder, truncated flare
NS	Navier-Stokes
PG	perfect gas
S	Sutherland's law
SDB	sharp, double cone
TE	thermal equilibrium
TLNS	thin-layer Navier-Stokes
TN	thermal nonequilibrium
U	unadapted grid

[†] Senior Research Engineer, Aerothermodynamics Branch, Associate Fellow AIAA

Copyright © 2001 by the American Institute of Aeronautics and Astronautics, Inc. No copyright is asserted in the United States under Title 17, U. S. Code. The U.S. Government has a royalty-free license to exercise all rights under the copyright claimed herein for Governmental Purposes. All other rights are reserved by the copyright owner.

Introduction

A series of numerical simulations were conducted of experiments performed in the LENS facility for the purpose of code validation under hypersonic conditions¹. The experiments were conceived to challenge simulation capabilities under conditions of large-scale separation while minimizing complicating factors associated with turbulence, gas chemistry, and three-dimensional end-effects. Experimental data will not be released until numerical simulations are reported on January 11, 2001².

The validation exercise here is similar to the First Europe-US High Speed Flow Field Database Workshop³. The hollow cylinder, truncated flare configuration was featured in that workshop where both the original experiment in R5Ch and several computational simulations were reported. More recently, experimental data and numerical simulations were reported⁴ of two, double-cone (25°/35° and 25°/50°) shock-shock interaction problems. The effective 10° compression case produced an Edney⁵ Type VI interaction, similar to the interaction observed here for the hollow-cylinder flare. The effective 25° compression case produced an Edney Type V interaction (with some allowance for viscous flow features) similar to the interaction produced here by the 25°/55° sharp, double cone.

The test conditions are closely related to the problem of predicting control surface effectiveness and heating at large deflection angles for access to space vehicles. The problem has been computationally investigated, for example, on the Space Shuttle⁶ and X-33⁷. The axisymmetric flow of the present test problems enables a much more comprehensive grid convergence study than possible on these more complex configurations.

Models

Schematics of the models and representative pressure fields are shown in Figures 1-3. Flow is from left to right. The sharp, double cone (SDC) model is shown in figure 1. The hollow cylinder, extended flare (HCEF) model is shown in figure 2 and the hollow cylinder, truncated flare (HCTF) is shown in figure 3. The leading edge of the hollow cylinder is sharp. Flow through the hollow cylinder is designed to pass through the model without influencing the external flow. The extended flare may allow larger separation as compared to the truncated flare in some cases where the shock impingement moves past the truncation height.

Test Conditions

Test conditions are presented in Table 1. Fundamental quantities in Table 1 (velocity, density, and temperature) are taken from the Calspan report;

Mach number and Reynolds number are derived from those quantities using appropriate thermodynamic and transport property relations for molecular nitrogen in the simulation code. All experiments were conducted in the Calspan-University at Buffalo Research Center (CUBRC) in the Large Energy National Shock (LENS) tunnel¹. Nominal flow conditions were at Mach 9.5 and Mach 11.5 with Reynolds numbers per meter from 140000 to 360000 in nitrogen. Steady, laminar, axisymmetric flow was reported for all tests considered here. Experimental data includes surface pressure and heating. This data will only be made available at the conclusion of the conference session on January 11, 2001².

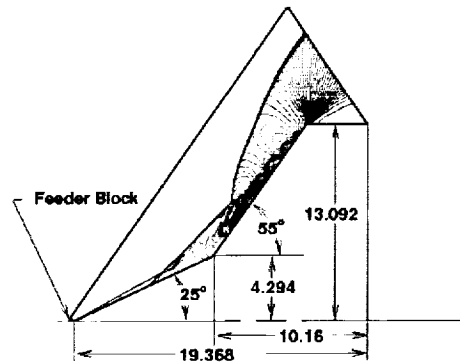


Figure 1: Sharp, double cone (SDC) and computational domain bounding pressure contour solution.

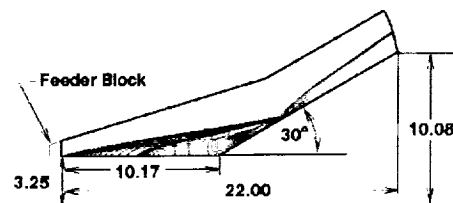


Figure 2: Hollow cylinder, extended flare (HCEF) and computational domain bounding pressure contour solution.

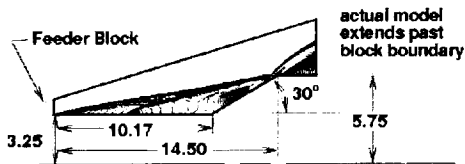


Figure 3: Hollow cylinder, truncated flare (HCTF) and computational domain bounding pressure contour solution.

Numerical Algorithm

Inviscid: The Langley Aerothermodynamic Upwind Relaxation Algorithm (LAURA)^{8,9} is used for all simulations in this report. Key elements of LAURA include Roe's averaging¹⁰ and Yee's Total Variation Diminishing (TVD)¹¹ formulation of second-order, inviscid fluxes. Yee's TVD formulation has been found to be exceptionally robust and Courant-number-independent using point-implicit relaxation for hypersonic flow simulations. The TVD algorithm uses a non-linear, minmod function as a flux limiter that maintains second-order accuracy away from extrema but can admit limit cycles in the convergence process, particularly in the vicinity of captured shocks. This occurrence usually manifests itself as a stalling of convergence at a very low error norm, essentially a benign ringing in the solution at a level that has no impact on aerothermodynamic quantities. However, the sharp, double cone test problem has proven to be more challenging than the typical application; the ringing has more profound consequences as will be discussed in the results section.

Viscous: Viscous flux is computed using central differences. A thin-layer, Navier-Stokes (TLNS) formulation is applied in both i and j coordinate directions. This formulation includes all but the cross derivative terms of the Navier-Stokes (NS) equation set. The complete NS equation set is also applied. Comparisons of TLNS and NS simulations show almost identical results for the test problems.

Gas Model: Perfect gas simulations for nitrogen specify $\gamma = 1.4$, $\mathcal{M} = 28.018$, $Pr = 0.71$, and Sutherlands law (S) for viscosity, $\mu = 1.3998 \cdot 10^{-6} T^{3/2} / (T + 106.667)$. Options for thermal equilibrium (TE) and

thermal nonequilibrium (TN) were also exercised for some simulations. In these options the gas is modeled as single species molecular nitrogen; the TE and TN specifications invoke thermodynamic curve fits for heat capacity and enthalpy as functions of temperature. Temperature in these tests is not high enough to promote significant dissociation of nitrogen. Transport properties in both the TE and TN options are derived from curve fits (C) of collision cross-sections for molecular nitrogen.

Thermal nonequilibrium is modeled using a two-temperature model. Translational and rotational energies are characterized by temperature T . Vibrational and electronic energies are characterized by temperature T_v . In the test problems considered here, vibrational and electronic energy modes are nearly frozen (except within the recirculation regions) making the constant γ perfect gas model a good approximation for the equation of state.

Grid: The computational domain for each configuration is included in figures 1-3. The outer boundary of each domain is initialized with straight lines from a point just upstream and above the leading edge of the model to an outflow boundary. The position of the boundary is designed to fully contain the shock. Grid lines emanating from the body of the SDC to the outer boundary are straight and parallel, at an angle normal to a reference line extending from the leading to trailing edge. The HCEF and HCTF configurations utilize a curvilinear grid that is normal to the body. Both the SDC and sharp leading edge hollow cylinder flare utilize a feeder block. The lower boundary of the feeder block is formed by the flow axis in the case of the SDC configuration and is an extension of the cylinder surface in the HCEF and HCTF configurations.

An exponential stretching function is used to distribute grid lines in the j direction from the body across the boundary layer and the shock. Cell Reynolds numbers less than 5 (HCEF, HCTF) or 11 (SDC) and maximum stretching factors less than or equal to 1.11 throughout the domain are within the LAURA parameter space for which heating in attached flows is expected to be grid converged. The experience base for stream wise resolution required to get grid converged separated flows is not sufficiently developed for apriori estimates of grid convergence.

In the hollow cylinder configurations a shock alignment algorithm in LAURA was used to bring the outer boundary in closer to the shock and make best use of grid resources. The alignment procedure in the SDC applications induced large-scale instabilities that did not damp out; the shock position would oscillate and waves would bounce off the outer boundary before it was re-adapted. Consequently, larger numbers of

grid in the j direction are required. The ranges of grid resources used are defined in Tables 2-4.

Boundary Conditions: Boundary conditions in LAURA require definition of variables within pseudo cell centers across the boundary. No-slip, cold-wall boundary conditions are used at the surface. Fixed, supersonic, inflow boundary conditions are applied at the outer ($j = j_{max}$) boundary and the $i = 1$ boundary of

the feeder block. Extrapolation is used across the predominantly supersonic outflow boundary. The $j = 1$ boundary of the feeder block uses an axis boundary condition in the case of the SDC and an extrapolation in the case of the hollow cylinder flares. Computed velocities remained parallel to this boundary using this specification.

Table 1: Test Problems

Model	Run	V_∞ , m/s	ρ_∞ , kg/m ³	T_∞ , K	T_w , K	M_∞	Re_∞ , m ⁻¹
HCEF	8	2667.	0.001206	132.8	296.7	11.35	359600.
HCEF	9	2566.	0.000845	121.1	296.7	11.44	264830.
HCEF	11	2609.	0.000507	128.9	297.2	11.27	152010.
HCEF	14	2432.	0.000794	156.1	295.6	9.55	185800.
HCTF	18	2661.	0.001175	130.6	295.6	11.42	355210.
SDC	24	2737.	0.001247	200.6	295.6	9.48	263790.
SDC	28	2664.	0.000655	185.6	293.3	9.59	144010.

Table 2: LAURA Cases for Run 8

Case	(I x J)	ϵ_i	Viscous	State	x_{sep}/L	Δs_{sep} , mm	x_{att}/L	Δs_{att} , mm
1	272 x 96, U	0.300	TLNS, S	PG	0.5203	0.722	1.3132	0.757
2	272 x 96, U	0.001	TLNS, S	PG	0.5202	0.722	1.3127	0.757
3	544 x 96, U	0.300	TLNS, S	PG	0.5269	0.362	1.3112	0.380
4	272 x 96, A	0.300	TLNS, S	PG	0.4650	0.734	1.3419	0.782
5	272 x 96, A	0.001	TLNS, S	PG	0.4810	0.732	1.3322	0.775
6	544 x 96, A	0.001	TLNS, S	PG	0.4736	0.367	1.3357	0.389
7	544 x 96, A	0.001	NS, S	PG	0.4708	0.367	1.3363	0.389
8	1088 x 96, A	0.001	NS, S	PG	0.4705	0.184	1.3373	0.195
9	1088 x 96, A*	0.001	NS, S	PG	0.4689	0.183	1.3329	0.194
10	544 x 96, A	0.001	TLNS, C	TE	0.5342	0.362	1.2994	0.376
11	544 x 96, A	0.001	TLNS, C	TN	0.4794	0.366	1.3266	0.385
12	1512 x 192, A	0.001	NS, S	PG	0.4410	0.184	1.3475	0.098

* A very small error in L equal to 0.28 mm out of 101.7016 mm was found and corrected after Case 8.

Table 3: LAURA Cases for Run 18

Case	(I x J)	ϵ_i	Viscous	State	x_{sep}/L	Δs_{sep} , mm	x_{att}/L	Δs_{att} , mm
1	272 x 96, U	0.001	NS, S	PG	0.5036	0.727	1.3170	0.771
2	272 x 96, A	0.001	NS, S	PG	0.4754	0.731	1.3330	0.781
3	544 x 96, A	0.001	NS, S	PG	0.4861	0.365	1.3280	0.389
4	1088 x 96, A	0.001	NS, S	PG	0.4840	0.182	1.3284	0.194
5	2176 x 192, A	0.001	NS, S	PG	0.4714	0.090	1.3352	0.096

Hollow Cylinder Flare Results

Overview: Five test conditions involving the hollow cylinder flare are defined in Table 1. The most comprehensive set of tests were executed for Run 8 on the HCEF configuration to investigate issues of grid convergence and effects of numerical parameters and gas models on the computed results as defined in Table 2. Case 1 was initialized with uniform flow. In all subsequent cases, solutions were initialized using earlier case converged solutions.

Grid convergence for the HCTF configuration in Run 18 was also investigated as defined in Table 3.

Pressure contours and streamlines for Run 8, Case 12 on the HCEF are shown in figure 4 over the cylinder and in figure 5 over the flare. The 30° flare sets up an oblique shock. The high post shock pressure is felt upstream through the boundary layer and induces separation. A weaker oblique shock sets up ahead of the separation point and the stronger flare shock moves further downstream with the

reattachment point. An equilibrium condition is established with separation at $x/L = 0.441$ and reattachment at $x/L = 1.348$. (In the case of the truncated flare, the equilibrium reattachment point may be constrained by the location of the truncation point). The separation shock overtakes the leading edge shock at approximately $x/L = 0.9$ in figure 4. Grid resolution in the vicinity of this interaction is approximately 0.1 mm in the stream wise direction and 0.2 mm in the normal direction. The shocks appear to merge into a single shock with the current available resolution. This separation shock intersects the flare shock at $x/L = 1.42$. Resolution in the vicinity of this interaction is approximately 0.1 mm in the stream wise direction and 0.03 mm in the normal direction.

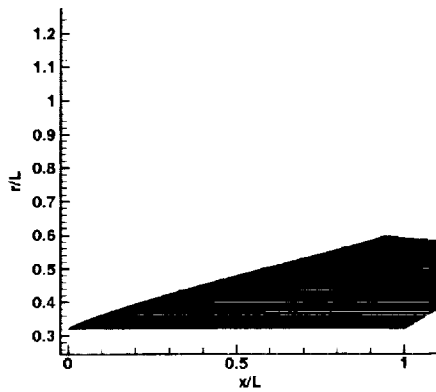


Figure 4: Pressure contours (flooded) and streamlines over cylinder part of HCEF for Run 8, Case 12.

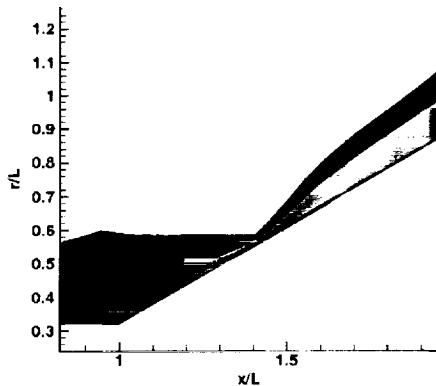


Figure 5: Pressure contours (flooded) and streamlines over flare part of HCEF for Run 8, Case 12.

In figure 4, a slight upwelling of the streamline in the reverse flow region near the wall at $x/L = 0.9$ is

observed. There is a local minimum in shear beneath this upwelling but there is no embedded, counter-rotating vortex in this simulation.

In Tables 2 and 3 the values of x_{sep}/L and x_{att}/L indicate locations of zero surface shear. The separation point follows the initial pressure rise by approximately 3 mm in Run 8. The variables Δs_{sep} and Δs_{att} in the tables indicate the stream wise mesh spacing across the separation and re-attachment points, respectively.

Case 12 uses the densest grid but suffered some ringing of the flux limiter so that the error norm stalled (order 10^{-3}). Case 9 results have the best combination of residual convergence (order 10^{-7}) and grid density. Using either Case 9 or 12 results as a reference in Table 2, it is evident that grid adaptation in coarser grids provides earlier separation and better agreement with the reference than unadapted results. For example, contrast Case 4 with Case 1 and Case 6 with Case 3.

Residual convergence: In all cases except Case 12, the L_2 error norm dropped to order 10^{-6} or lower. Case 12 residual convergence stalled at an L_2 error norm of order 10^{-3} for 128 hours of single processor R12000 CPU time. In contrast, Case 8 required 100 point-implicit relaxation steps and 5660 line-implicit relaxation steps for 16.3 CPU hours to drop the L_2 error norm to $3.1 \cdot 10^{-7}$. (In general, these test cases with large separation and fine stream wise grids are more susceptible to ringing of the flux limiter and require smaller Courant numbers to reduce ringing. The sharp double cone results section includes additional discussion on this issue of stalled convergence.)

Eigenvalue limiter: The eigenvalue limiter provides positive definite dissipation in the upwind scheme when Roe averaged eigenvalues on an i face are less than $2\epsilon_i$. (Limiters in the j direction spanning the boundary layer utilize an additional reduction factor.) The limiting is only engaged in regions where there is flow reversal or near-sonic velocity. Expansion shocks are admitted without the limiter. Previous experience with attached, fully supersonic flow indicates that the smaller limiter provides more accurate solutions on coarser grids while the larger values of the limiter enhance solution robustness. Little effect is seen in the unadapted grid between Case 1 and 2. A 1.6 mm difference (approximately two stream wise cells) in the separation point is observed for the adapted, coarse grid result (Case 4 versus Case 5). The larger eigenvalue limiter in this comparison provides better agreement with the Case 12 reference, in contradiction to previous experience as noted above. Subsequent cases retain use of the smaller value ($\epsilon_i = .001$) in keeping with prior experience. The separation point for Run 12 on the

finest grids occur within the same cell for $\epsilon_1 = 0.001$ or 0.300.

Physical models: The additional cross derivative terms included in Case 7 for the NS equation set provide insignificant (within 1 stream wise cell) difference in location of the separation point as compared to the TLNS equation set of Case 6.

The thermal equilibrium option for single species nitrogen engages the curve fits for heat capacity, including effects of vibrational excitation ignored in the perfect gas (PG) model. It also engages curve fits for collision cross section (C) to compute transport properties rather than using Sutherland's law (S) and constant Prandtl number in the PG model. When vibrational excitation is included under conditions of thermal equilibrium (Case 10) a decrease in separation extent is observed (~6 mm) as compared to the PG mode (Case 6). However, when thermal nonequilibrium effects are included (Case 11) the vibrational temperature stays relatively low, vibrational energy modes are not significantly populated, and the constant γ approximation of the PG model is more accurate. In this situation, the onset of separation for the TN model (Case 11) is only about 0.6 mm delayed as compared to the PG model (Case 6).

Comparison of cases 6, 10, and 11 for surface pressure coefficient and Stanton number are presented in Figures 6-9. They confirm on a global and detailed basis the near equivalence of the PG and TN models for conditions of Run 8.

Influence of Mach Number and Reynolds Number: Runs 8, 9, and 11 exhibit a variation in Reynolds number at approximately constant Mach number 11.3. Surface pressure coefficient and Stanton number for these three runs using consistent grids, gas model, and numerical parameters from Case 9 are compared in figures 10-14. The extent of separation increases with increasing Reynolds number. The over-expansion on the flare is more pronounced at the higher Reynolds number (Run 8).

The influence of Mach number is investigated by comparing Run 14 at Mach 9.5 to Runs 9 and 11 at Mach 11.4. The free stream Reynolds numbers for Runs 9 and 11 bound the Run 14 Reynolds number. The extent of separation for Run 14 is also bounded by the extent of separation for Runs 9 and 11, as shown in figures 10-14. The effect of Mach number over this limited range appears to be much less significant than the effect of Reynolds number.

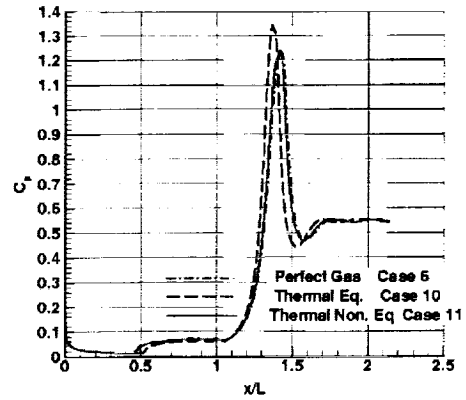


Figure 6: Surface pressure coefficient (global view) over HCEF from Run 8 showing effect of thermodynamic model.

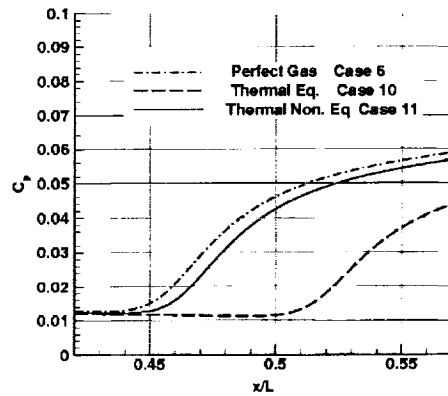


Figure 7: Detail from figure 6 around separation point.

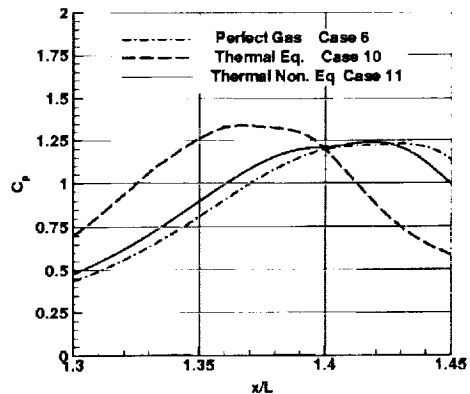


Figure 8: Detail from figure 6 around attachment point.

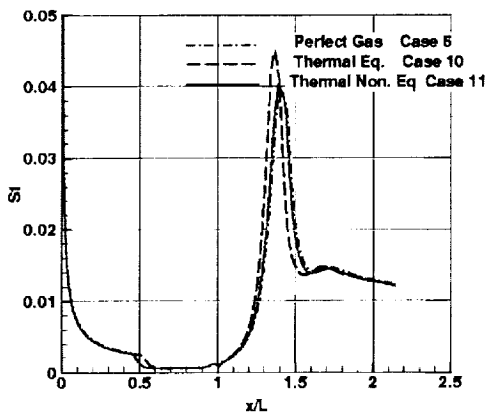


Figure 9: Stanton number (global view) over HCEF from Run 8 showing effect of thermodynamic model.

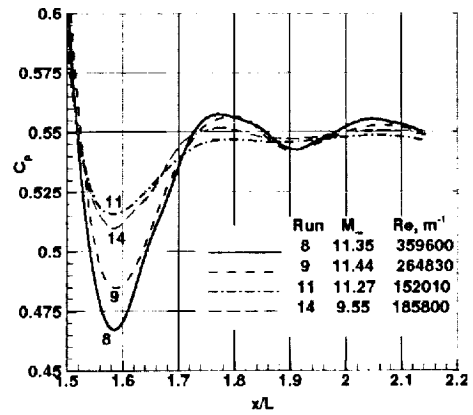


Figure 12: Detail from figure 11 showing magnitude of over-expansion and reflected waves.

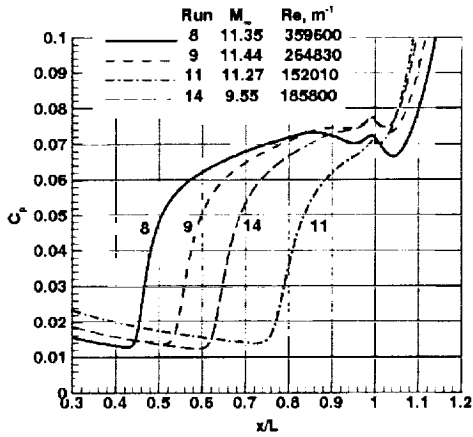


Figure 10: Influence of Reynolds number and Mach number on pressure coefficient over HCEF cylinder.

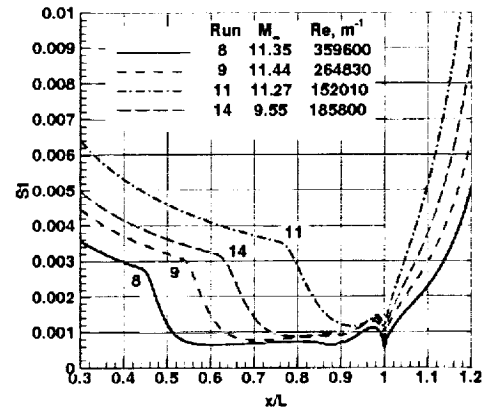


Figure 13: Influence of Reynolds number and Mach number on Stanton number over HCEF cylinder.

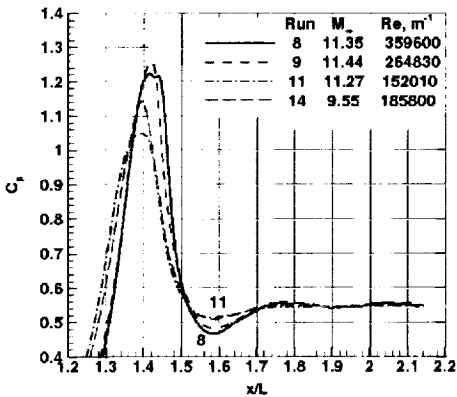


Figure 11: Influence of Reynolds number and Mach number on pressure coefficient over HCEF flare.

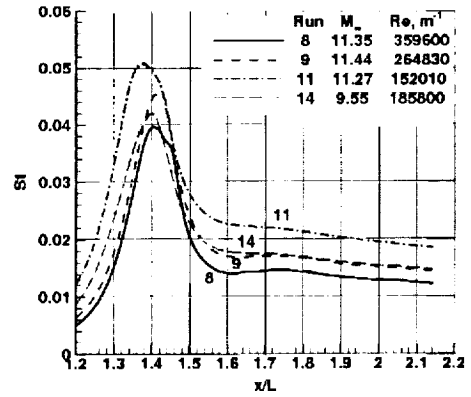


Figure 14: Influence of Reynolds number and Mach number on Stanton number over HCEF flare.

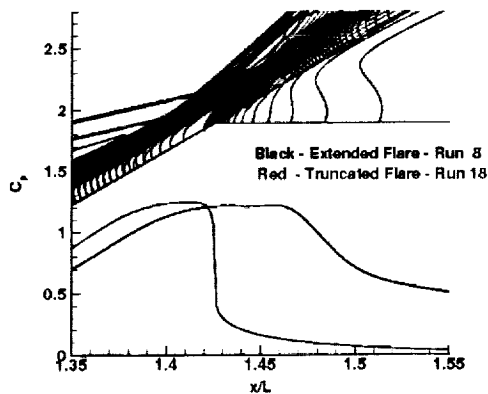


Figure 15: Surface pressure coefficient distribution and overlay of pressure coefficient contours from Run 8 (black) and Run 18 (red) around peak pressure.

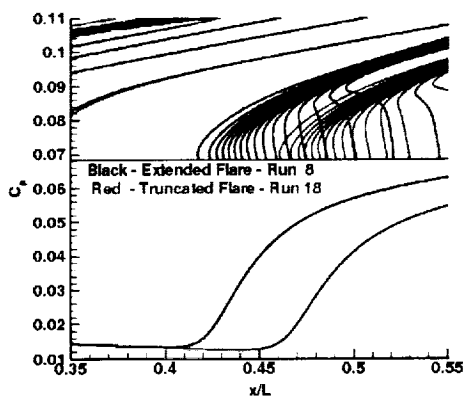


Figure 16: Surface pressure coefficient distribution and overlay of pressure coefficient contours from Run 8 (black) and Run 18 (red) around peak pressure point.

Truncated Flare Effect: The attachment point for Run 8, the largest Reynolds number test, on the extended flare is situated approximately 8 mm upstream of the corresponding truncated flare expansion corner. The peak pressure for Run 8 below the shock-shock interaction is located on the extended flare at the equivalent location of the expansion corner on the truncated flare. Run 18 over the truncated flare has equivalent Mach and Reynolds numbers as Run 8. The attachment point for Run 18 is constrained by the expansion corner; flow relief through expansion at this corner reduces the extent of separation. This point is illustrated in figure 15 in which pressure contours in the vicinity of the attachment point for Run 8 (Case 12) and Run 18 (Case 5) are compared. The corresponding pressure

contours at the separation point are presented in figure 16.

Grid Convergence: Grid convergence of surface pressure coefficients and Stanton number using equivalent physical models and numerical parameters are documented in figures 17-20 for Run 8 (HCEF). Figure 17 features a global view of C_p convergence as a function of grid density. Figures 18 and 19 focus on the separation and attachment points. Only a global view of Stanton number convergence as a function of grid is presented because relative differences follow the same trend as presented in corresponding figures for C_p . Also, corresponding figures for Run 18 are similar to Run 8 results and are not presented. Runs 8 and 18 are at nearly equivalent free stream conditions.

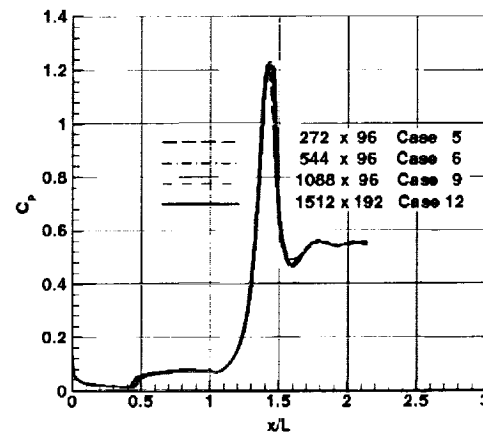


Figure 17: Surface pressure coefficient as function of grid resolution for Run 8 over HCEF.

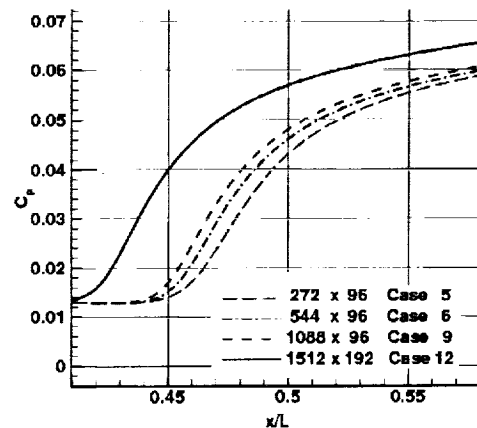


Figure 18: Detail of figure 17 around separation point.

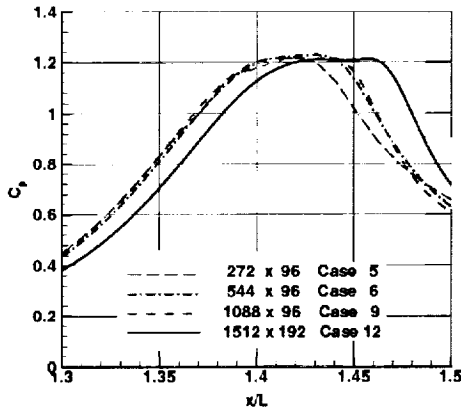


Figure 19: Detail of figure 17 near attachment point.

Both grid convergence tests exhibit residual convergence for the first three grid densities (272 x 96), (544 x 96), and (1088 x 96); both experience stalling of convergence for the finest grids (1544 x 192) in Run 8 and (2176 x 192) in Run 18. Stream wise grid convergence is evident for the three cases with 96 points across the shock layer. A subsequent refinement across the shock layer (192 points)

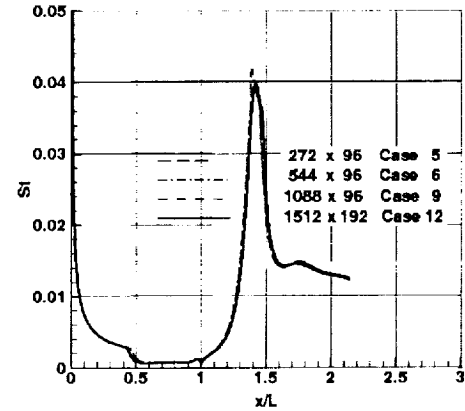


Figure 20: Stanton number as function of grid resolution for Run 8 over HCEF.

induces a slight, earlier onset of separation but low-level oscillations are not damped and the residuals fail to converge. There is no large-scale motion evident in the hollow cylinder flare cases when the residual hangs in this manner. However, this behavior is more profound in the SDC tests described in the next section.

Table 4: LAURA Cases for Run 28

Case	(I x J)	ϵ_i	Viscous	State	x_{sep}/L	Δs_{sep} , mm	x_{att}/L	Δs_{att} , mm
1*	64 x 64, U	0.300	TLNS, S	PG	0.7676	3.70	1.083	3.91
2*	128 x 128, U	0.300	TLNS, S	PG	0.7974	1.85	1.0779	1.96
3*	256 x 128, U	0.300	TLNS, S	PG	0.6540	0.926	1.1841	0.978
4*	256 x 128, U	0.300	NS, S	PG	0.6505	0.926	1.1841	0.978
5*	512 x 256, U	0.300	TLNS, S	PG	0.5580	0.463	1.2790	0.489
6*	512 x 256, A	0.300	TLNS, S	PG	0.5634	0.463	many	
7	512 x 256, U	0.300	NS, S	PG	0.5713	0.463	1.281	0.489
8	1024 x 256, U	0.001	NS, S	PG	0.5555	0.231	1.291	0.245
9	512 x 256, U	0.001	TLNS, C	TN	0.7176	0.463	1.147	0.489
10	512 x 256, U	0.001	TLNS, C	TN**	0.7209	0.463	1.145	0.489
11	512 x 256, U	0.001	TLNS, C	TE	0.8410	0.463	1.084	0.489
12	512 x 256, U	0.001	TLNS, S	TN	0.7013	0.463	1.159	0.489
13	512 x 256, U	0.001	NS, S	TN	0.6944	0.463	1.161	0.489

* Used preliminary conditions: $V_\infty = 2658$ m/s, $\rho_\infty = 0.000778$ kg/m³, $T_\infty = 198.9$ K

** $T_{v,\infty} = 1000$ K

Sharp, Double-Cone Results

Overview: Two test conditions involving the sharp, double cone (SDC) are defined in Table 1. The most comprehensive set of tests were executed for Run 28 on the SDC configuration to investigate issues of grid convergence and effects of numerical parameters and gas models on the computed results as defined in Table 4. Case 1 was initialized with uniform flow. In all subsequent cases, solutions were initialized using earlier case converged solutions.

Pressure shaded contours and streamlines for Run 28, Case 8, are shown in figure 21 focusing on the interaction region surrounding the cone-cone junction. The flow develops in much the same way as described previously for the HCEF. The relative 30° angle of the second cone to the first is the same angle as the HCEF and HCTF tests. The separation shock sets up on the first cone at $x/L \sim 0.55$. The separated flow extends from this point to $x/L \sim 1.3$ on the second cone. The dividing streamline sits

approximately half way between the junction point and the shock. Unlike the HCEF simulations, a counter-rotating vortex sets up within the larger separation bubble above the cone-cone junction. A complex series of interacting shocks and expansions sets up downstream of the shock-shock interaction and the termination of the separation bubble. Figures 22 and 23 will focus on these interactions.

Figure 22 shows pressure, streamlines, and sonic line in a view that zooms in on the interaction region. The dividing streamline of the separation region is slightly concave, forming a compression boundary in the region $1.1 < x/L < 1.25$. Compression waves focus to the center of the shock layer where they interact with a shock emanating from the shock-shock interaction. The interaction of these two waves appears to form a Mach disk, behind which a subsonic, high-pressure zone is formed, bounded by two transmitted shocks. (Details of these structures are somewhat muted by grid resolution of 0.14 mm by 0.24 mm in this region.) The upward running shock reflects as an expansion off the dividing streamline passing through the shock-shock interaction point. This streamline bounds an approximately constant pressure region and closely follows the sonic line. The downward running wave terminates on the tail of the recirculation zone. There is an expansion off the tail of the recirculation zone that ultimately reflects from the upper dividing streamline / slip surface containing the sonic line. Subsequent wave reflections continue in the expected manner; compression waves reflect from solid boundaries as compressions and reflect from constant pressure surfaces as expansions. Expansion waves reflect from solid boundaries as expansions and from constant pressure surfaces as compressions¹².

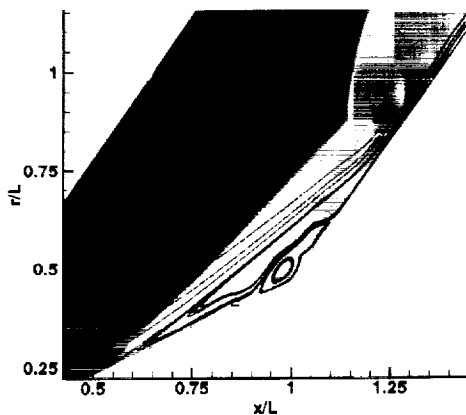


Figure 21: Pressure contours (flooded) and streamlines over interaction region of SDC for Run 28, Case 8.

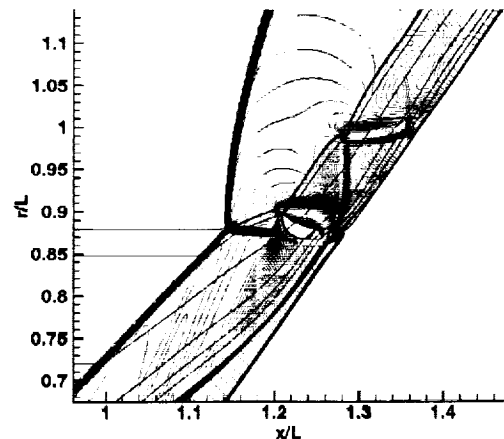


Figure 22: Detail of interaction region for Run 28 with pressure contours (thin, multi-colored lines), streamlines (thin, black lines), and sonic line (thick, red line).

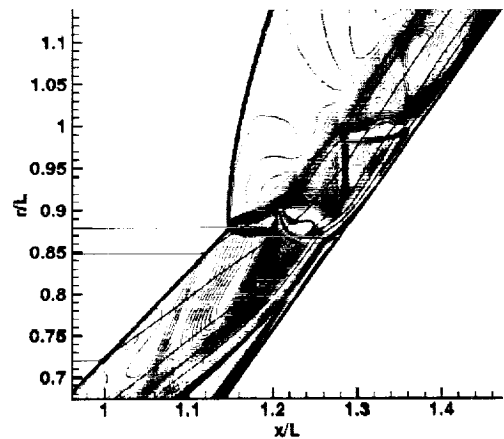


Figure 23: Detail of interaction region for Run 28 with density contours (thin, multi-colored lines), streamlines (thin, black lines), and sonic line (thick, red line).

Figure 23 highlights the slip surface emanating from the shock-shock interaction using density contours. The high-density gradient defines the viscous slip surface; it contains the dividing streamline and sonic line. Flow is supersonic beneath the slip surface and subsonic above it.

The test cases for Run 28 in Table 4 are chosen to demonstrate grid convergence and test effects of physical models and numerical parameters. Effects of eigenvalue limiter and choice of TLNS or NS

equation sets have minimal impact on results, consistent with observations for the HCEF. Grid convergence studies and tests involving thermal nonequilibrium models exhibited behaviors not observed in the HCEF tests; these behaviors are discussed in the following sections.

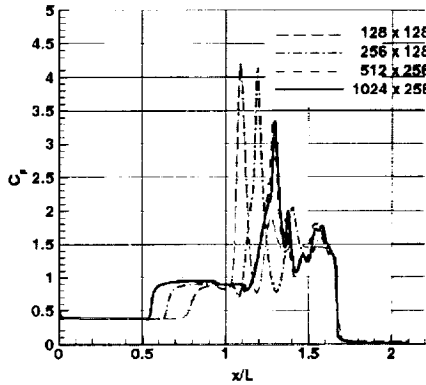


Figure 24: Grid convergence study for Run 28 – surface pressure coefficient.

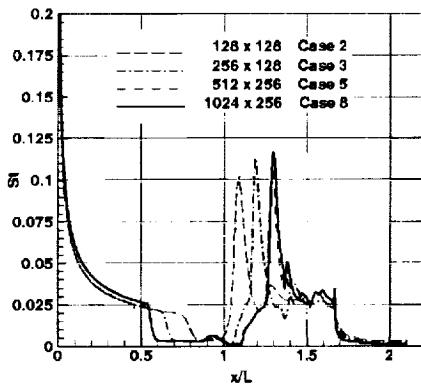


Figure 25: Grid convergence study for Run 28 – Stanton number.

Grid and Residual Convergence: Grid convergence trends for Run 28 are documented in figure 24 (C_p) and in figure 25 (St). The separation point moves forward as grid is refined, consistent with trends observed in the HCEF tests. The complex, reflected wave pattern noted in figures 22 and 23 causes multiple peaks and valleys downstream of reattachment. The final stream wise doubling of grid produces negligible change in surface pressure or heating. A subsequent attempt to double the grid in the normal direction initiated slight, upstream movement of the separation; however, the separation bubble became highly unstable and the large-scale

motion would never damp out. Repeated attempts to nurse the solution by decreasing Courant number, changing order of relaxation sweeps, or using more conservative relaxation factors would delay but not eliminate the problem.

The cause of this numerical unsteadiness is unknown. Such large-scale motions were not detected experimentally. In general, the minmod operator used in the flux limiter to obtain 2nd-order accuracy away from discontinuities could possibly serve as a disturbance source that is amplified by this specific combination of algorithm and flow physics. The minmod function compares three characteristic gradients in the neighborhood of a cell wall; the function makes discrete choices regarding which argument to return depending on relative magnitudes and signs. While the minmod function is known to occasionally introduce ringing in the residual convergence in the vicinity of shocks (due to cycling of the returned argument) a problem of inducing major unsteadiness has not been observed previously in LAURA applications. This issue is further explored in the simulation of Run 24 while examining effect of Reynolds number.

Effect of Reynolds Number: The effect of Reynolds number is explored by comparing Run 24 with Run 28. As noted in Table 1, the Reynolds number for Run 24 is nearly double that of Run 28. Based on experience with HCEF trends, the separation point for Run 24 would be expected to move upstream. The Run 24 simulation was initialized from Run 28, Case 7, and used the same grid and numerical parameters to generate the solution. The separation point was observed to move upstream, approaching $x/L = 0.4$. As the simulation continued large-scale unsteadiness developed, just as observed in Run 28 albeit on a much finer grid.

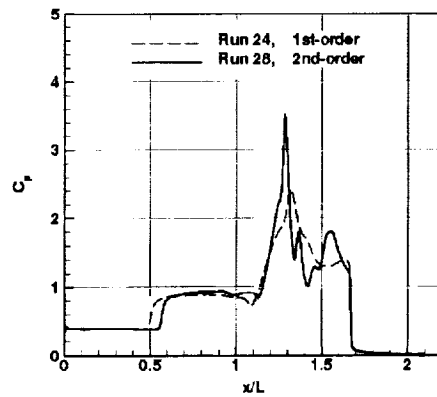


Figure 26: Comparison of surface pressure coefficient including combined effect of Reynolds number and order of accuracy.

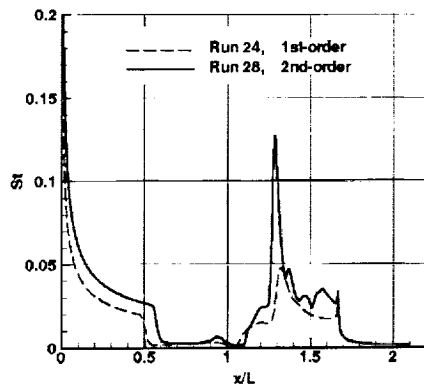


Figure 27: Comparison of Stanton number including combined effect of Reynolds number and order of accuracy.

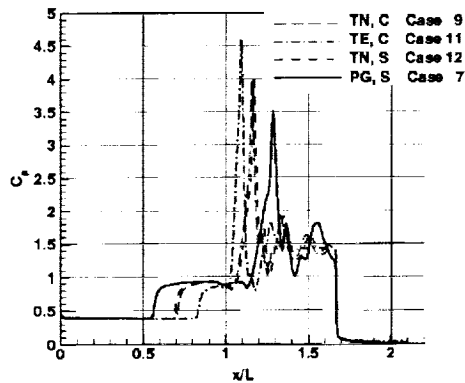


Figure 28: Effect of thermodynamic and transport property models on surface pressure coefficient for Run 28.

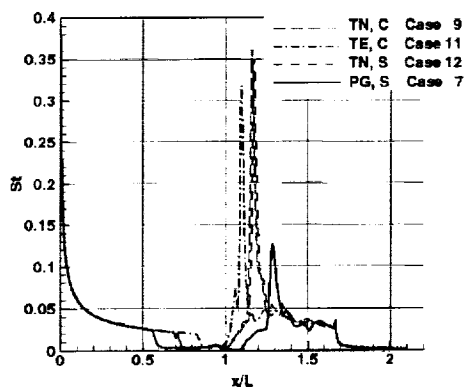


Figure 29: Effect of thermodynamic and transport property models on Stanton number for Run 28.

Since the higher-order treatment is suspected of inducing the instabilities a simulation for Run 24 was made that included only the 1st order flux differencing. This solution converged and is compared to Run 28 in figures 26 and 27. The separation point for the higher Reynolds number case occurs earlier than the lower Reynolds number case. It is assumed that the difference in separation location would be larger if both simulations were 2nd-order accurate.

Effect of Gas Model: A comparison of perfect gas, thermal equilibrium and thermal nonequilibrium gas models for Run 28 are presented in figures 28 and 29. A comparison of the viscosity models is also included, revealing no significant difference between the Sutherland's law and N₂ collision cross section curve fits when used in conjunction with the same thermodynamic model (Case 9 and Case 12).

The thermal equilibrium simulation shows significant reduction in separation extent, even larger than observed with HCEF results in figures 6 and 9. At thermal equilibrium temperatures, vibrational energy modes are engaged and the simulation would not be expected to match the constant γ , perfect-gas results.

The thermal nonequilibrium simulation shows larger extent of separation than the thermal equilibrium case in figures 28 and 29. This result is consistent with HCEF results in figures 6 and 9. Vibrational temperatures are essentially frozen at free stream levels, except for slight increases in the recirculation region and farther downstream over the expansion corner. The ratio of specific heats is effectively constant and yet agreement with perfect gas results is poor, unlike the HCEF results.

The Roe's averaging algorithm involves additional quantities for the general case of thermochemical nonequilibrium. It is at first glance surprising that these small algorithm differences could support such a large difference in separation extent; especially considering that good agreement in the HCEF tests was obtained. A plot of pressure contours, streamlines, and sonic line for Case 9 (not shown) equivalent to figure 22 indicates the absence of the subsonic cove. In this case, there appears to be a regular reflection rather than Mach reflection. The approach of the dividing streamline to the surface is smoother at the tail of the recirculation bubble. If this test is at the cusp of conditions where subtle changes can support either regular or Mach reflection beneath the shock-shock interaction then the observed differences for very similar gas models and supporting algorithms may be credible.

Summary

A series of numerical simulations were conducted of experiments performed in the LENS facility for the purpose of code validation under hypersonic conditions. The experiments were conceived to challenge simulation capabilities under conditions of large-scale separation while minimizing complicating factors associated with turbulence, gas chemistry, and three-dimensionality. Experimental data will not be released until numerical simulations are reported.

Nominal test conditions are at Mach 9.5 and 11.4 at Reynolds numbers varying from 144000 to 360000 per meter. Three axisymmetric models are considered in this report. Two hollow cylinders with sharp leading edges and 30° flares are studied in the first series of tests. A truncated flare slightly limited extent of separation for the highest Reynolds number tested. A sharp, double cone (25°/55°), including a 30° compression is studied in the second series of tests. The models are roughly 20 cm in length and 13 to 26 cm in diameter.

Numerical simulations show increasing extent of separation with increasing Reynolds number and

significant movement of the separation point over the tested range. Mach number was not a significant factor affecting separation for the limited range considered here. All simulations required finer grids than what might be considered "intuitively" expected in order to achieve grid converged results.

The hollow cylinder results exhibited very slight increase in separation between the two finest grids tested. Residual convergence was generally good, though some tests showed convergence that stalled, probably due to the non-linear minmod limiter. The sharp, double cone results at the lowest Reynolds number appeared to show grid convergence, but massive instabilities manifested when an additional level of refinement was introduced. The highest Reynolds number double cone test required 1st-order dissipation in order to get any convergence. Very complex wave reflections were observed in the double cone tests. A possibility of supporting either regular reflection or Mach reflection was noted which might explain sensitivity of results to grid and physical models.

References

- ¹ "Experimental Database from CUBRC Studies in Hypersonic Laminar and Turbulent Interacting Flows including Flowfield Chemistry," Prepared for RTO Code Validation of DSMC and Navier-Stokes Code Validation Studies, Calspan-University at Buffalo Research Center, Buffalo, NY, June 2000.
- ² Holden, M. and Harvey, J.: "Comparisons Between Experimental Measurements over Cone/Cone and Cylinder /Flare Configurations and Predictions Employing DSMC and Navier-Stokes Solvers," AIAA 2001-1031, January 2001.
- ³ Borrelli, S.; Grasso, F.; Marini, M.; Periaux, J. (eds.): Proceedings of The First Europe-US High Speed Flow Field Database Workshop, Part II, Naples, Italy, November 12-14, 1997, © C. I. R. A. (Italy), distributed by AIAA, ISBN 1-56347-341-0.
- ⁴ Wright, M. J.; Sinha, K.; Olejniczak, J.; Candler, G. V.; Magruder, T. D.; Smits, A. J.: "Numerical and Experimental Investigation of Double-Cone Shock Interactions," AIAA Journal, Vol. 38, No. 12, Dec. 2000, pp 2268,2276.
- ⁵ Edney, Barry: "Anomalous Heat Transfer and Pressure Distributions on Blunt Bodies at Hypersonic Speeds in the Presence of an Impinging Shock," FFA Report 115, Flygtekniska Försöksanstalten (Aeronautical Research Institute of Sweden), Stockholm, 1968.
- ⁶ Weilmuenster, K. J.; Gnoffo, P. A.; and Greene, F. A.: "Navier-Stokes Simulations of Orbiter Aerodynamic Characteristics Including Pitch Trim and Bodyflap," JSR, Vol. 31, No. 3, 1994, pp. 355-366.
- ⁷ Gnoffo, P. A.; Weilmuenster, K. J.; Hamilton II, H. H.; Olynick, D. R.; Venkatapathy, E.: "Computational Aerothermodynamic Design Issues for Hypersonic Vehicles," JSR, Vol. 36, No. 1, 1999, pp. 21-43.
- ⁸ Gnoffo, P. A.; Gupta, R. N.; and Shinn, J.: "Conservation Equations and Physical Models for Hypersonic Air Flows in Thermal and Chemical Nonequilibrium," NASA TP 2867, 1989.
- ⁹ Cheatwood, F. M. and Gnoffo, P. A. "Users Manual for the Langley Aerothermodynamic Upwind Relaxation Algorithm (LAURA)," NASA TM 4674, April 1996.
- ¹⁰ Roe, P. L.: "Approximate Riemann Solvers, Parameter Vectors, and Difference Schemes," Journal of Computational Physics, Vol.43, Oct. 1981, pp357-372.
- ¹¹ Yee, H. C.: "On Symmetric and Upwind TVD Schemes," NASA TM-88325, June 1986.
- ¹² Shapiro, A. H.: The Dynamics and Thermodynamics of Compressible Fluid Flow Vol. 1, The Ronald Press Company, New York, 1953, pp 451-453.

